

## Preparation of MWCNT-MnO<sub>2</sub>/Ni foam composite electrode for electrochemical degradation of Congo red wastewater

Huajing Zhu\* and Zeli Chen

School of Biology and Environmental Engineering, Tianjin Vocational Institute, Tianjin 300410, China

\*E-mail: [huajingzhu1866@163.com](mailto:huajingzhu1866@163.com)

Received: 3 January 2021 / Accepted: 20 February 2021 / Published: 31 March 2021

---

Dye wastewater has the characteristics of high chroma, strong toxicity and difficult degradation, which has a serious impact on the environment. Because of its advantages of low energy consumption, simple operation and no secondary pollution, electrochemical oxidation technology has been increasingly studied in the field of refractory organic wastewater treatment. In this work, we report a multiwalled carbon nanotube (MWCNT)-MnO<sub>2</sub> nanocomposite as a Ni foam electrode modification. Then, the MWCNT-MnO<sub>2</sub>/Ni electrode is used for the electrochemical oxidation of Congo red dye. We study the effect of various factors on the decolorization of Congo red by the single-factor method. The results show that the decolorization rate of Congo red decreases with an increasing initial concentration and pH. In this work, hydroxyl radicals are detected by high-performance liquid chromatography. In the case of hydroxyl radicals and chloride ions acting separately, it is concluded that the indirect oxidation of chloride ions is the main mechanism during the process of electrocatalytic oxidation.

---

**Keywords:** Electrochemical oxidation; Congo red; Nanocomposite; Degradation mechanism; Multi-walled carbon nanotube

### 1. INTRODUCTION

With the rapid growth of the world economy, the printing and dyeing industry has become one of the fastest growing industries. However, the production of dye wastewater during the process of printing and dyeing has a serious impact on the environment because of its high chroma, strong toxicity, potential for harm and difficult degradation [1–6]. The treatment rate of dye wastewater is very low, only 30%, and only 60% of the total treatment amount can meet the discharge requirements after treatment. Due to the above characteristics of dye wastewater and its serious impact on the environment, it has become an urgent problem to find an efficient and treatment method with low energy consumption [7–11].

The adsorption method is the most widely used physical treatment method in the process of dye wastewater treatment. Its principle is to add a large number of porous substances into dye wastewater to fully mix with the dye wastewater and then adsorb macromolecular organic pollutants during the mixing process to purify the wastewater. The treatment effect of the adsorption method is generally related to the adsorbent, dye type, dye structure, solubility, reaction time, temperature and other factors [12–16]. The reaction effects of different dyes and adsorbents are different. The adsorption method has the advantages of small investment, less land occupation and simple operation. However, its efficiency is low, and if the saturated adsorbent is not treated properly, it easily causes secondary pollution to the environment. The main principle of treating dye wastewater by membrane separation is to use the selective permeability of a membrane. When wastewater passes through a specific treatment membrane, a part of the material will be intercepted due to the selectivity of the membrane [17–20]. The concentration and recovery of intercepted dye macromolecules can not only purify wastewater but also recycle the dye. As membrane separation technology does not need to add chemicals to the treatment system, it will not cause secondary pollution to the environment. The operation is simple and convenient, and the dye can be separated and recovered from the separation process. However, the defect of the membrane treatment method is that the membrane will continue to scale and block in the process of treatment, so it needs to be cleaned or replaced [21–23]. Moreover, the treatment of dye wastewater requires a membrane with high acid and alkali resistance and corrosion resistance, so this method is generally suitable for the advanced treatment of wastewater.

The main principle of electrocatalytic oxidation is to produce hydroxyl radicals or other strong oxidizing substances under the action of an external electric field to oxidize and degrade macromolecular organic pollutants in water to small molecules or directly mineralize them into  $\text{CO}_2$  and  $\text{H}_2\text{O}$ , thus removing organic pollutants from the wastewater. In the electrocatalytic oxidation system, different anode materials lead to different reaction mechanisms. The material and characteristics of the anode directly determine the reaction method and effect. Traditional graphite electrodes and lead alloy electrodes have the advantages of good conductivity and low price, but they easily passivate and corrode during the reaction process, resulting in a poor degradation effect [24–29]. It is a complex subject to study the degradation mechanism of organic pollutants by electrocatalytic oxidation technology because there are many factors affecting the electrolysis mechanism that will change with changes in the electrode materials, electrolysis conditions, electrolytes and other factors.

In this work, we prepare a multiwalled carbon nanotube- $\text{MnO}_2$  nanocomposite for use as a Ni foam modification. Then, the prepared electrode is used for the electrochemical oxidation of Congo red dye. We analyse the effects of various factors on the decolorization and degradation of Congo red. Then, the samples are analysed by ion chromatography and LC-MS to infer the possible degradation process.

## 2. MATERIALS AND METHODS

MWCNTs were purchased from Nanjing Tianchen Technology Co., Ltd. The average size is approximately 20  $\mu\text{m}$ . Ni foam with a diameter of 30 mm was purchased from Linchen Yemen

Technology Co., Ltd. All other reagents were purchased from Aladdin Biotech Co., Ltd. These reagents were used without further purification.

The MWCNTs were first treated by acidification (1:3 = HNO<sub>3</sub>:H<sub>2</sub>SO<sub>4</sub>). Then, 0.2 g of the MWCNTs was added to 100 mL of water and sonicated for half an hour. Next, 50 mL of MnSO<sub>4</sub> (10 mM) and (NH<sub>4</sub>)<sub>2</sub>S<sub>2</sub>O<sub>8</sub> was introduced into the MWCNT dispersion. The mixture was then stirred for 3 h. Next, the mixture was moved to a hydrothermal pot at 120 °C overnight and cooled naturally. The MWCNT-MnO<sub>2</sub> composite was then collected after the washing process. Pure MnO<sub>2</sub> was prepared using a similar method without the addition of MWCNTs.

Either the MWCNTs, MnO<sub>2</sub> or MWCNT-MnO<sub>2</sub> composite was used for the Ni foam modification. First, acetylene black and polytetrafluoroethylene were mixed with either the MWCNTs, MnO<sub>2</sub> or MWCNT-MnO<sub>2</sub> composite to form a coating ink at a ratio of 1:1:5. Then, the coating ink was coated on the Ni foam. Next, the coated electrode was dried at room temperature overnight.

The morphologies of the samples were studied by SEM (MIRA3 TESCAN). EDS (energy dispersive spectrometry) analysis was investigated by an XL30 Philips microscope. XRD was investigated using an X'PertPro instrument with a monochromatized Cu K $\alpha$  radiation source ( $\lambda = 1.54 \text{ \AA}$ ). Infrared absorption spectra were recorded using FTIR spectroscopy.

Before the experiment, 100 mg/L Congo red solution was prepared as the reserve solution. In each experiment, 500 mL of Congo red solution was poured into a beaker, a certain amount of sodium chloride powder was weighed and dissolved in the solution, and the pH of the solution was adjusted with an acidimeter. After adjusting the solution, the beaker was placed on a magnetic stirrer. The electrode plate was the anode, and Ti was the cathode. After the beginning of the electrolysis reaction, 8 mL samples were taken at regular intervals and stored in a refrigerator at 4 °C for subsequent analysis.

In this experiment, the decolorization rate was used as an index to judge the difficulty of decolorization and degradation. The calculation formula is as follows:

$$\alpha = \frac{(A_0 - A_t)}{A_0} \times 100$$

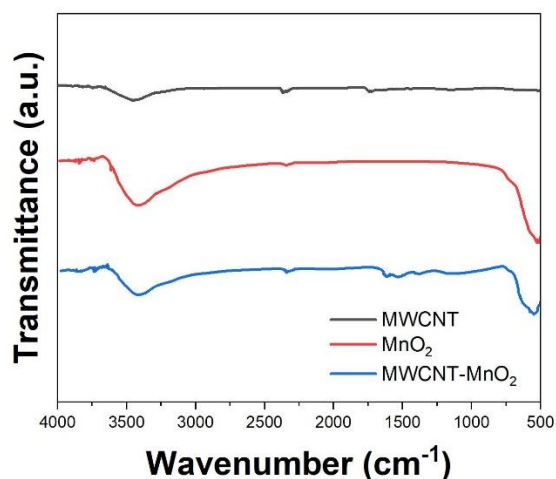
where A<sub>0</sub> and A<sub>t</sub> are the initial absorbance of the solution and the absorbance after reaction time t, respectively.

The maximum absorption wavelength of Congo red was 570 nm under acidic conditions. Its maximum absorption wavelength was 496 nm under alkaline and neutral conditions.

### 3. RESULTS AND DISCUSSION

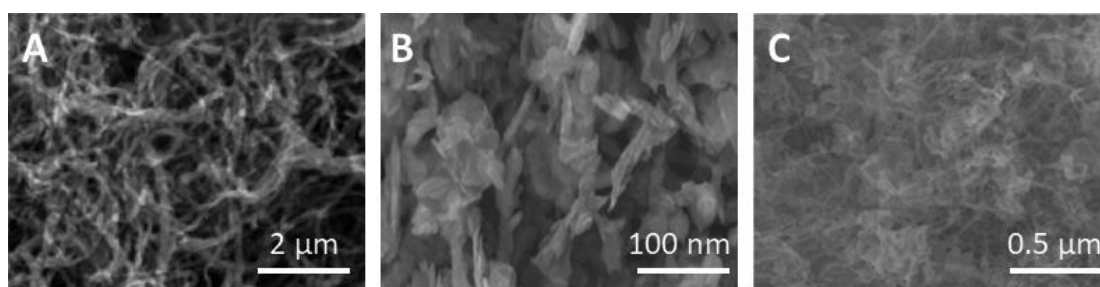
FTIR was used to characterize the surface functional groups on the materials. Figure 1 shows the FTIR spectra of the MWCNTs, MnO<sub>2</sub> and the MWCNT-MnO<sub>2</sub> composite. The MWCNTs have a peak at 1680 cm<sup>-1</sup>, which corresponds to the C=O stretching band of -COOH [30,31]. In addition, the peaks at 3450 cm<sup>-1</sup> and 1083 cm<sup>-1</sup> correspond to hydroxyl groups and C-O bond stretching, respectively [32,33]. Moreover, the bands at 2910 and 2850 cm<sup>-1</sup> can be assigned to the CH stretching and -CH<sub>2</sub> groups, respectively. The spectrum of MnO<sub>2</sub> exhibits a distinct peak at approximately 500 cm<sup>-1</sup> due to Mn-O. The spectrum of the MWCNT-MnO<sub>2</sub> composite shows both features, suggesting the successful

formation of the composite. In addition, some blueshifts are observed due to the combination. These blueshifts can be explained by the change in metal complexes depending on the coordination structures.



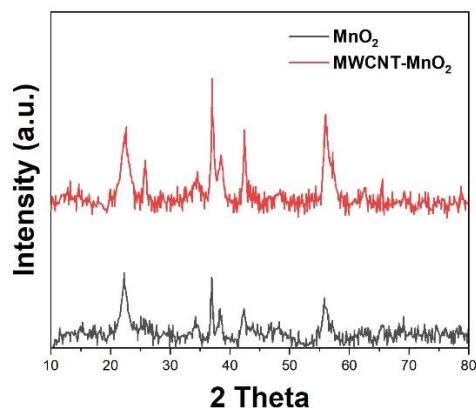
**Figure 1.** FTIR spectra of the MWCNTs, MnO<sub>2</sub> and MWCNT-MnO<sub>2</sub> composite (recorded using powders of the materials).

Figure 2 shows SEM images of the MWCNTs, MnO<sub>2</sub> and MWCNT-MnO<sub>2</sub> composite. The MWCNTs shows a typical wire morphology, while MnO<sub>2</sub> shows a layered structure with an average size of 50 nm. The incorporation of MWCNTs into MnO<sub>2</sub> slightly changes the morphology of MnO<sub>2</sub>. MnO<sub>2</sub> shows an irregular shape. This result may be because the MWCNTs prevent MnO<sub>2</sub> from growing along a specific crystal plane. We can see from the figure that nanocomposites have been successfully synthesized.



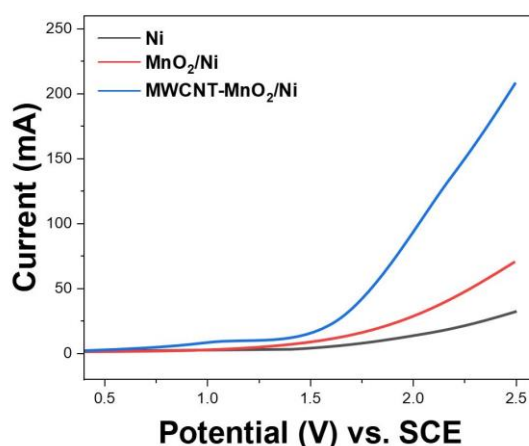
**Figure 2.** SEM images of the (A) MWCNTs, (2) MnO<sub>2</sub> and (3) MWCNT-MnO<sub>2</sub> composite (recorded using powders of the materials on conductive tape).

Figure 3 shows the XRD patterns of MnO<sub>2</sub> and the MWCNT-MnO<sub>2</sub> composite. It can be seen from the figure that the XRD pattern of the MWCNT-MnO<sub>2</sub> composite shows an extra peak located at 25.6° compared with that of the XRD pattern of MnO<sub>2</sub>. This strong peak can be ascribed to the (002) plane of the MWCNTs, suggesting the successful formation of the MWCNT-MnO<sub>2</sub> composite. Other peaks at 22.27°, 34.51°, 36.79°, 38.27°, 42.31° and 56.12° can be indexed to the (120), (031), (131), (230), (300) and (160) planes of γ-MnO<sub>2</sub> [34–36].



**Figure 3.** XRD patterns of MnO<sub>2</sub> and the MWCNT-MnO<sub>2</sub> composite (recorded using powders of the materials).

Figure 4 shows the linear sweep voltammetry of Ni, MnO<sub>2</sub>/Ni and MWCNT-MnO<sub>2</sub>/Ni in 0.5 M Na<sub>2</sub>SO<sub>4</sub> solution for investigating the oxygen evolution overpotential. The oxygen evolution overpotentials of Ni, MnO<sub>2</sub>/Ni and MWCNT-MnO<sub>2</sub>/Ni are all approximately 1.50 V, indicating that the modification of the MnO<sub>2</sub> or MWCNT-MnO<sub>2</sub> composite does not increase the oxygen evolution overpotential. In contrast, the oxygen evolution current changes significantly. More specifically, MnO<sub>2</sub>/Ni shows a higher oxygen evolution current than Ni. The modification of MWCNT-MnO<sub>2</sub> further enhances the oxygen evolution current, suggesting that the MWCNT-MnO<sub>2</sub> composite has a much larger surface area than the bare Ni foam [37,38], which is beneficial for the degradation of dye molecules.



**Figure 4.** Linear sweep voltammetry of Ni, MnO<sub>2</sub>/Ni and MWCNT-MnO<sub>2</sub>/Ni in 0.5 M Na<sub>2</sub>SO<sub>4</sub> (0.1 M NaCl, scan rate: 50 mV/s).

Figure 5 shows the electrochemical oxidation of Congo red at the different electrodes. As shown in the figure, none of the electrodes have any oxidation peak in the absence of Congo red, suggesting that all electrodes are inactive in Na<sub>2</sub>SO<sub>4</sub>. In contrast, all three electrodes show oxidation peaks when 200 mg/L Congo red is present, suggesting that the oxidation of Congo red can occur at any of the tested electrodes. In addition, no reduction peak can be observed, indicating that all three electrodes can be

used for the oxidative degradation of Congo red. The oxidation potentials of Congo red at Ni, MnO<sub>2</sub>/Ni and MWCNT-MnO<sub>2</sub>/Ni are 1.230 V, 1.151 V and 1.076 V, respectively. These results indicate that MWCNT-MnO<sub>2</sub>/Ni has the highest electrooxidation activity towards Congo red [39,40].

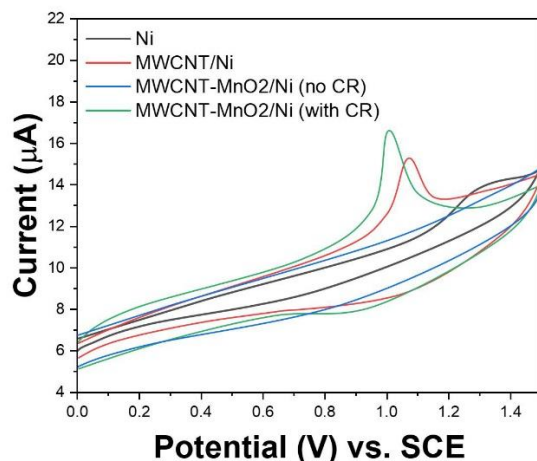


**Figure 5.** Cyclic voltammetry of Ni, MnO<sub>2</sub>/Ni and MWCNT-MnO<sub>2</sub>/Ni in 0.5 M Na<sub>2</sub>SO<sub>4</sub> in the presence of 200 mg/L Congo red (0.1 M NaCl, scan rate: 50 mV/s).

Figure 6A shows the effect of the initial Congo red concentration on degradation. The initial concentrations of Congo red are 50 mg/L, 100 mg/L, 150 mg/L, 200 mg/L and 250 mg/L. The electrolysis time is 2 h. The effect of the initial concentration of Congo red on decolorization and degradation is not notable. When the initial concentration of Congo red wastewater increases, the decolorization rate decreases, but the decrease range is small [41]. The decolorization rate is between 85% and 91%. When the initial concentration of Congo red is low, the solution begins to change colour after electrolysis. When the reaction lasts for approximately 5 min, the solution begins to turn yellow, and the decolorization rate is more than 80%. However, when the initial concentration of Congo red increases to 150 mg/L, the reaction begins to slow down. The solution slowly changes from blue-purple to reddish-brown, and then to red and finally to yellowish-brown. The whole discoloration process is relatively slow, and the decolorization rate can reach approximately 80% only after approximately 10 min of electrolysis.

The pH value directly reflects the hydrogen ion activity in the solution, so it has an important influence on the solution reaction [42]. Figure 6B shows the effect of different initial pH values on the decolorization and degradation of Congo red. It can be seen from the figure that the effect of the initial pH value on the decolorization and degradation of Congo red is obvious. The decolorization rate of the Congo red solution decreases with the change in initial pH from acidic to alkaline. When the initial pH of Congo red is 3, the reaction rate is very fast after electrolysis [43]. With an increasing alkalinity, the reaction begins to slow down, and the final decolorization rate decreases. Therefore, when the initial pH of the solution is acidic, the decolorization rate can reach more than 80% after 5 min of electrolysis. When the initial pH increases to alkaline, the reaction slows down, and the final decolorization rate decreases. When the pH value of the solution changes, the surface charge of the electrode will also

change [44]. When the acidity of the solution is different, the degree of  $\text{Cl}^-$  adsorption on the anode is different.  $\text{Cl}^-$  is a strong oxidant in the reaction process.

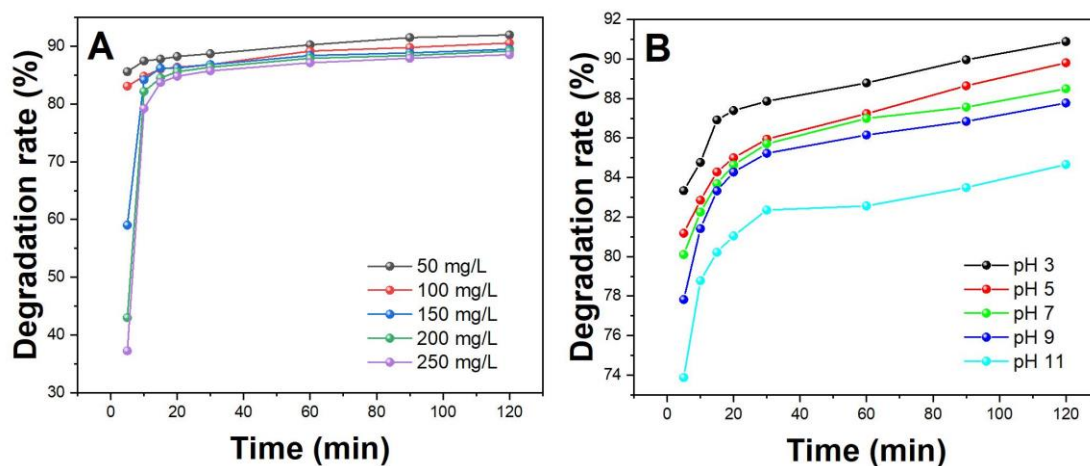


**Figure 6.** Effect of the (A) initial concentration of Congo red and (B) pH on decolorization performance. Degradation conditions: 0.5 M  $\text{Na}_2\text{SO}_4$  (0.1 M  $\text{NaCl}$ ); 1.2 V.

Table 1 illustrates a comparison between the synthesized MWCNT- $\text{MnO}_2/\text{Ni}$  foam composite electrode in this study and other reported literature for the degradation of Congo red. By considering the degradation time, the synthesized MWCNT- $\text{MnO}_2/\text{Ni}$  foam composite displays better or comparable degradation efficiency.

**Table 1.** Comparison of between the degradation performances of electrodes for degradation of methyl orange.

Electrode	Applied voltage	Degradation efficiency (%)	Degradation time (min)	Ref.
Graphene oxide	1.5 V	88	110	[45]
Boron-doped diamond anode	-	95	80	[46]
$\text{Ag}_2\text{O}$ /Spring mud	1.2 V	77	120	[47]
Graphite	-	95	150	[48]
Polyaniline/ $\text{TiO}_2$	2.0 V	97	120	[49]
MWCNT- $\text{MnO}_2/\text{Ni}$ foam composite	1.2 V	92	90	This work

By detecting the ions in the sample after electrolysis by ion chromatography, we can determine which groups in the organic structure are replaced [50]. After analysing the wastewater solution sample after electrolysis by ion chromatography, an ion chromatogram of the 180 min sample was obtained, as

shown in Figure 7A.  $\text{NO}_3^-$ ,  $\text{SO}_3^{2-}$  and  $\text{SO}_4^{2-}$  ions are produced from the Congo red wastewater by electrolytic oxidation. Among them, the content of  $\text{NO}_3^-$  is lower and the content of  $\text{SO}_4^{2-}$  is the highest. After 3 h,  $\text{Cl}^-$  still exists in the solution. During the electrolysis process,  $\text{NO}_3^-$ ,  $\text{SO}_3^{2-}$  and  $\text{SO}_4^{2-}$  ions are produced within 10 min, but their amounts are small. As the electrolysis reaction proceeds, the yields of these ions gradually increase, indicating that the amino groups of the organic matter are replaced and oxidized to  $\text{NO}_3^-$  during the electrolysis process [51]. The sulfonic group is substituted to form  $\text{SO}_3^{2-}$ . Part of the  $\text{SO}_3^{2-}$  content continues to be oxidized to  $\text{SO}_4^{2-}$ . Figure 7B shows the possible degradation mechanism of Congo red on the electrode surface. This mechanism is similar to the oxidation of hydroxyl-substituted azo dye [52].

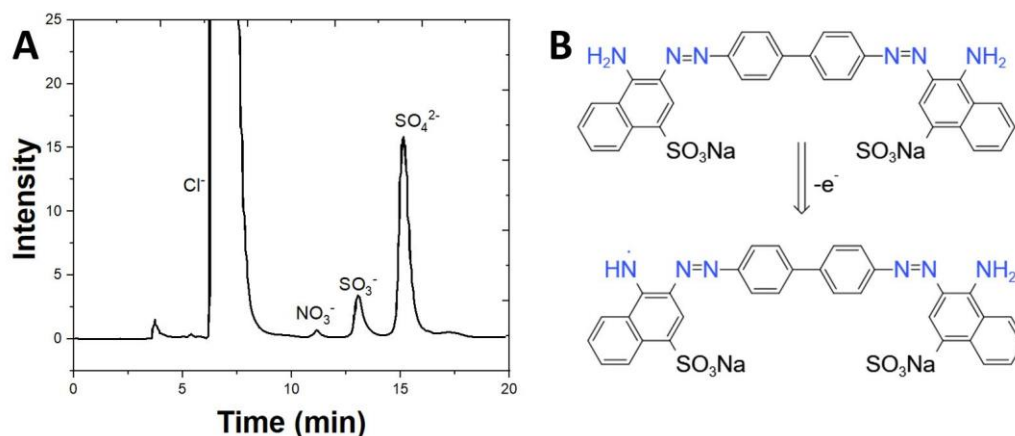


**Figure 7.** (A) Ion chromatogram of the sample after 180 min of electrochemical oxidation. (B) Possible mechanism of the oxidation of Congo red.

In this experiment, there are two kinds of strong oxidizing substances that lead to the degradation of macromolecular organic matter, namely, hydroxyl radicals and active chlorine. To understand the degradation mechanism, it is necessary to determine the strong oxidizing substances that play a key role in the pulsed electrocatalytic oxidation system. Hydroxyl radicals play a very important role in electrochemical treatment [53]. Whether hydroxyl radicals are produced in pulsed electrocatalytic oxidation will directly affect the degradation mechanism of Congo red. In this experiment, salicylic acid is used to capture hydroxyl radicals, and the main products are 2,3-dihydroxybenzoic acid and 2,5-dihydroxybenzoic acid [54]. The products can be detected by HPLC to indirectly detect the generation of hydroxyl radicals during the electrolysis process.

The chromatographic results of salicylic acid with electrolysis time are shown in Figure 8A. 2,3-Dihydroxybenzoic acid and 2,5-dihydroxybenzoic acid are produced from salicylic acid by electrolysis. The yield concentration increases with the electrolysis time, but the ratio of each product concentration remains unchanged [55]. The concentration of 2,5-dihydroxybenzoic acid is always approximately 5 times that of 2,3-dihydroxybenzoic acid. This result is because the distribution of electron clouds on the benzene ring affects the formation of the two products. Other substances detected in the figure may be

the byproducts of salicylic acid during electrolysis [56]. The experimental results show that hydroxyl radicals will be produced in the electrolysis system, and the concentration will increase over time.

In the electrolysis system, hydroxyl radicals and chloride ions are two kinds of strong oxidizing substances that can play the role of oxidative degradation. To understand the mechanism of electrolysis, hydroxyl radicals and chloride ions should react separately, and their effects should be compared to determine which substance is dominant in the electrolysis process [57]. To verify the effect of the hydroxyl radical reaction under acidic, neutral and basic conditions, the reaction pH was adjusted to 3, 7 and 11. Figure 8B analyses the decolorization rate of Congo red over time under different pH conditions to observe the electrolysis effect. When hydroxyl radicals acted alone, the decolorization rate of Congo red increases gradually with an increasing electrolysis time, but the electrolysis effect is not obvious. After electrolysis for one hour, the output of bubbles is very small, the colour of the solution has no obvious change, and the decolorization rate is less than 20%. Within half an hour before electrolysis, the decolorization rate of Congo red under alkaline conditions is slightly higher than that under acidic and neutral conditions [58]. However, in the second half hour, the decolorization rate reaches its highest point under acidic conditions. Notably, the decolorization rate of a Congo red solution is very low under acidic, neutral or alkaline conditions. Under acidic conditions, the content of hydroxyl radicals increases with an increasing electrolysis time, so the decolorization rate increases gradually. Under alkaline conditions, the growth rate of hydroxyl radicals first increases and then decreases. Therefore, the decolorization rate increases rapidly in the early stage and decreases in the later stage. During the whole electrolysis process, the concentration of hydroxyl radicals is very low, so the decolorization effect of Congo red is not good when hydroxyl radicals act alone.

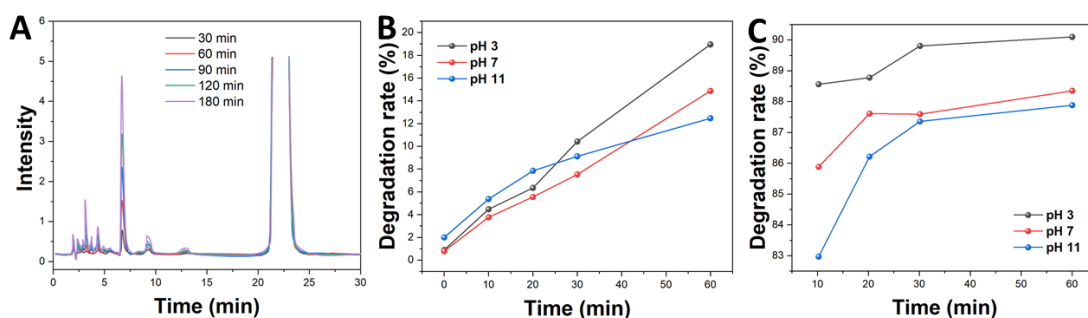


**Figure 8.** (A) HPLC chromatogram of the salicylic acid electrolysis sample. (B) Change in decolorization rate over time under different pH conditions. (C) Change in decolorization rate over time under different pH values when chloride ions acted alone.

When  $\text{Cl}^-$  exists in the reaction system, the degradation of Congo red is accomplished by  $\text{Cl}^-$  and hydroxyl radicals. To judge the role of  $\text{Cl}^-$  in the degradation of Congo red, it is necessary to screen hydroxyl radicals during electrolysis [59]. In the study of electrochemical reactions of hydroxyl radicals, organic alcohols are often used as scavengers for hydroxyl radicals because they are excellent electron donors. Figure 8C shows that a better decolorization effect can be achieved after electrolysis for 10 min under the action of chloride ions alone. After electrolysis for 1 h, the decolorization rate reaches more

than 80%. In the electrocatalytic oxidation system, chloride ions play two main roles [60]. One is as an electrolyte, which improves the conductivity of the solution and reduces energy consumption [61]. Second, as an electrode reactant because it is oxidized to form chlorine gas after electron loss at the anode, thus producing active chlorine such as HClO and ClO<sup>-</sup>.

#### 4. CONCLUSION

In this work, we prepared a MWNCT-MnO<sub>2</sub> nanocomposite for use as a Ni foam modification. Then, MWCNT-MnO<sub>2</sub>/Ni was used for the electrochemical oxidation of Congo red. We investigated the effect of various factors on the decolorization of Congo red in the process of electrolytic treatment. First, the effects of various factors on the decolorization rate of Congo red were studied by the single-factor method. According to the results of the single-factor experiment, the response surface curve was analysed, and the optimal reaction conditions were obtained and optimized. Then, we studied the degradation products and degradation pathway of Congo red in the electrocatalytic oxidation system. The degradation mechanism of Congo red was determined by HPLC.

#### ACKNOWLEDGMENT

This work was supported by the Scientific Research Fund of Tianjin Vocational Institute (20171105).

#### References

1. V. Selvaraj, T.S. Karthika, C. Mansiya, M. Alagar, *J. Mol. Struct.* (2020) 129195.
2. E. Routoula, S.V. Patwardhan, *Environ. Sci. Technol.*, 54 (2020) 647–664.
3. G. Singh, M. Sharma, R. Vaish, *Adv. Powder Technol.*, 31 (2020) 1771–1775.
4. Z. Sabouri, A. Akbari, H.A. Hosseini, M. Darroudi, *J. Mol. Struct.*, 1173 (2018) 931–936.
5. H. Karimi-Maleh, F. Karimi, S. Malekmohammadi, N. Zakariae, R. Esmaeili, S. Rostamnia, M.L. Yola, N. Atar, S. Movaghgharnezhad, S. Rajendran, A. Razmjou, Y. Orooji, S. Agarwal, V.K. Gupta, *J. Mol. Liq.*, 310 (2020) 113185.
6. H. Karimi-Maleh, F. Karimi, M. Alizadeh, A.L. Sanati, *Chem. Rec.*, 20 (2020) 682–692.
7. M. Mohsin, I.A. Bhatti, A. Ashar, A. Mahmood, Q. ul Hassan, M. Iqbal, *J. Mater. Res. Technol.*, 9 (2020) 4218–4229.
8. F. Ijaz, S. Shahid, S.A. Khan, W. Ahmad, S. Zaman, *Trop. J. Pharm. Res.*, 16 (2017) 743–753.
9. C.V. Reddy, I.N. Reddy, B. Akkinapally, V. Harish, K.R. Reddy, S. Jaesool, *Ceram. Int.*, 45 (2019) 15298–15306.
10. L. Fu, Z. Liu, J. Ge, M. Guo, H. Zhang, F. Chen, W. Su, A. Yu, *J. Electroanal. Chem.*, 841 (2019) 142–147.
11. J. Zhou, Y. Zheng, J. Zhang, H. Karimi-Maleh, Y. Xu, Q. Zhou, L. Fu, W. Wu, *Anal. Lett.*, 53 (2020) 2517–2528.
12. H. Karimi-Maleh, M. Alizadeh, Y. Orooji, F. Karimi, M. Baghayeri, J. Rouhi, S. Tajik, H. Beitollahi, S. Agarwal, V.K. Gupta, S. Rajendran, S. Rostamnia, L. Fu, F. Saberi-Movahed, S. Malekmohammadi, *Ind. Eng. Chem. Res.*, 60 (2021) 816–823.
13. H. Karimi-Maleh, Y. Orooji, A. Ayati, S. Qanbari, B. Tanhaei, F. Karimi, M. Alizadeh, J. Rouhi, L. Fu, M. Sillanpää, *J. Mol. Liq.* (2020) 115062.

14. B. Mandal, J. Panda, P.K. Paul, R. Sarkar, B. Tudu, *Vacuum*, 173 (2020) 109150.
15. Y. Wang, H. Yang, X. Sun, H. Zhang, T. Xian, *Mater. Res. Bull.*, 124 (2020) 110754.
16. Y. Zhao, S. Kang, L. Qin, W. Wang, T. Zhang, S. Song, S. Komarneni, *Chem. Eng. J.*, 379 (2020) 122322.
17. S. Vasantharaj, S. Sathiyavimal, M. Saravanan, P. Senthilkumar, K. Gnanasekaran, M. Shanmugavel, E. Manikandan, A. Pugazhendhi, *J. Photochem. Photobiol. B*, 191 (2019) 143–149.
18. Y. Hunge, A. Yadav, V. Mathe, *Ultrason. Sonochem.*, 45 (2018) 116–122.
19. H. Karimi-Maleh, A. Ayati, R. Davoodi, B. Tanhaei, F. Karimi, S. Malekmohammadi, Y. Orooji, L. Fu, M. Sillanpää, *J. Clean. Prod.*, 291 (2021) 125880.
20. L. Fu, Y. Zheng, P. Zhang, H. Zhang, M. Wu, H. Zhang, A. Wang, W. Su, F. Chen, J. Yu, W. Cai, C.-T. Lin, *Bioelectrochemistry*, 129 (2019) 199–205.
21. L. Fu, A. Wang, K. Xie, J. Zhu, F. Chen, H. Wang, H. Zhang, W. Su, Z. Wang, C. Zhou, S. Ruan, *Sens. Actuators B Chem.*, 304 (2020) 127390.
22. N.Y. Nadaf, S.S. Kanase, *Arab. J. Chem.*, 12 (2019) 4806–4814.
23. X. Cao, H. Wang, S. Zhang, O. Nishimura, X. Li, *Chemosphere*, 208 (2018) 219–225.
24. H. Karimi-Maleh, B.G. Kumar, S. Rajendran, J. Qin, S. Vadivel, D. Durgalakshmi, F. Gracia, M. Soto-Moscoso, Y. Orooji, F. Karimi, *J. Mol. Liq.*, 314 (2020) 113588.
25. L. Di, H. Yang, T. Xian, X. Chen, *Micromachines*, 9 (2018) 613.
26. K. Sathiyar, R. Bar-Ziv, O. Mendelson, T. Zidki, *Mater. Res. Bull.*, 126 (2020) 110842.
27. A. Wahab, M. Imran, M. Ikram, M. Naz, M. Aqeel, A. Rafiq, H. Majeed, S. Ali, *Appl. Nanosci.*, 9 (2019) 1823–1832.
28. Y. Xu, Y. Lu, P. Zhang, Y. Wang, Y. Zheng, L. Fu, H. Zhang, C.-T. Lin, A. Yu, *Bioelectrochemistry*, 133 (2020) 107455.
29. M. Zhang, B. Pan, Y. Wang, X. Du, L. Fu, Y. Zheng, F. Chen, W. Wu, Q. Zhou, S. Ding, *ChemistrySelect*, 5 (2020) 5035–5040.
30. W. Zhong, T. Jiang, Y. Dang, J. He, S.-Y. Chen, C.-H. Kuo, D. Kriz, Y. Meng, A.G. Meguerdichian, S.L. Suib, *Appl. Catal. Gen.*, 549 (2018) 302–309.
31. M. Ajaz, S. Shakeel, A. Rehman, *Int. Microbiol.*, 23 (2020) 149–159.
32. M. Bilal, T. Rasheed, H.M. Iqbal, H. Hu, W. Wang, X. Zhang, *Int. J. Biol. Macromol.*, 113 (2018) 983–990.
33. M.R. Ladole, P.B. Pokale, S.S. Patil, P.G. Belokar, A.B. Pandit, *Bioresour. Technol.*, 317 (2020) 124035.
34. J. Zhao, J. Nan, Z. Zhao, N. Li, J. Liu, F. Cui, *Appl. Catal. B Environ.*, 202 (2017) 509–517.
35. F.W. Boyom-Tatchemo, F. Devred, G. Ndiffo-Yemeli, S. Laminsi, E.M. Gaigneaux, *Appl. Catal. B Environ.*, 260 (2020) 118159.
36. S. Panimalar, R. Uthrakumar, E.T. Selvi, P. Gomathy, C. Inmozhi, K. Kaviyarasu, J. Kennedy, *Surf. Interfaces*, 20 (2020) 100512.
37. X. Luo, H. Liang, F. Qu, A. Ding, X. Cheng, C.Y. Tang, G. Li, *Chemosphere*, 200 (2018) 237–247.
38. H. Yasmeen, A. Zada, S. Liu, *J. Photochem. Photobiol. Chem.*, 380 (2019) 111867.
39. W.-K. Jo, S. Kumar, M.A. Isaacs, A.F. Lee, S. Karthikeyan, *Appl. Catal. B Environ.*, 201 (2017) 159–168.
40. D. Iark, A.J. dos Reis Buzzo, J.A.A. Garcia, V.G. Côrrea, C.V. Helm, R.C.G. Corrêa, R.A. Peralta, R. de F.P.M. Moreira, A. Bracht, R.M. Peralta, *Bioresour. Technol.*, 289 (2019) 121655.
41. S.T. Fardood, F. Moradnia, A. Ramazani, *Micro Nano Lett.*, 14 (2019) 986–991.
42. N. Ali, A. Said, F. Ali, F. Raziq, Z. Ali, M. Bilal, L. Reinert, T. Begum, H.M. Iqbal, *Water. Air. Soil Pollut.*, 231 (2020) 1–16.
43. S. Sathiyavimal, S. Vasantharaj, M. Shanmugavel, E. Manikandan, P. Nguyen-Tri, K. Brindhadevi, A. Pugazhendhi, *Prog. Org. Coat.*, 148 (2020) 105890.
44. S.D. Khairnar, M.R. Patil, V.S. Shrivastava, *Iran. J. Catal.*, 8 (2018) 143–150.

45. N.P. Shetti, S.J. Malode, R.S. Malladi, S.L. Nargund, S.S. Shukla, T.M. Aminabhavi, *Microchem. J.*, 146 (2019) 387–392.
46. H. Jalife-Jacobo, R. Feria-Reyes, O. Serrano-Torres, S. Gutiérrez-Granados, J.M. Peralta-Hernández, *J. Hazard. Mater.*, 319 (2016) 78–83.
47. C. Merah, *Malays. J. Anal. Sci.*, 24 (2020) 266–275.
48. R. Kaur, H. Kaur, *Port. Electrochimica Acta*, 34 (2016) 185–196.
49. K.M. Emran, S.M. Ali, A. Al-Oufi, *Int J Electrochem Sci*, 13 (2018) 5085–5095.
50. U. Habiba, J.J.L. Lee, T.C. Joo, B.C. Ang, A.M. Afifi, *Int. J. Biol. Macromol.*, 131 (2019) 821–827.
51. M.U. Khalid, S.R. Khan, S. Jamil, *J. Inorg. Organomet. Polym. Mater.*, 28 (2018) 168–176.
52. M.B. Shekardasht, M.H. Givianrad, P. Gharbani, Z. Mirjafary, A. Mehrizad, *Diam. Relat. Mater.*, 109 (2020) 108008.
53. S.S.R. Albeladi, M.A. Malik, S.A. Al-thabaiti, *J. Mater. Res. Technol.*, 9 (2020) 10031–10044.
54. G.-E. Yuan, Y. Li, J. Lv, G. Zhang, F. Yang, *Biochem. Eng. J.*, 120 (2017) 118–124.
55. R. Arunadevi, B. Kavitha, M. Rajarajan, A. Suganthi, A. Jeyamurugan, *Surf. Interfaces*, 10 (2018) 32–44.
56. M.A. Iqbal, S.I. Ali, F. Amin, A. Tariq, M.Z. Iqbal, S. Rizwan, *ACS Omega*, 4 (2019) 8661–8668.
57. M.A. Salem, E.A. Bakr, H.G. El-Attar, *Spectrochim. Acta. A. Mol. Biomol. Spectrosc.*, 188 (2018) 155–163.
58. R. Das, M. Bhaumik, S. Giri, A. Maity, *Ultrason. Sonochem.*, 37 (2017) 600–613.
59. G.B. Jegadeesan, S. Amirthavarshini, J. Divya, G. Gunarani, *Adv. Powder Technol.*, 30 (2019) 2890–2899.
60. A.M. Mohammed, S.S. Mohtar, F. Aziz, M. Aziz, A. Ul-Hamid, W.N.W. Salleh, N. Yusof, J. Jaafar, A.F. Ismail, *Mater. Sci. Semicond. Process.*, 122 (2021) 105481.
61. J. Srivind, V. Nagarethinam, M. Suganya, S. Balamurugan, D. Prabha, A. Balu, *Mater. Sci. Eng. B*, 255 (2020) 114530.